Jpn. J. Appl. Phys. Vol. 38 (1999) pp. 1730–1741
Part 1, No. 3B, March 1999


# A High Performance Doppler Interferometer for Advanced Optical Storage Systems

Chih-Kung LEE[1,*1], Giin-Yuan WU[2,*2], Chao-Ting TENG[2], Wen-Jong WU[1], Chi-Ting LIN[1], Wen-Hsing HSIAO[1], Hsieh-Chin SHIH[1], Jen-Shung WANG[1], San-Chien LIN[2], Chan Ching LIN[2], Ching-Fa LEE[2] and Yen-Chen LIN[2]

[1]*Institute of Applied Mechanics, National Taiwan University, No. 1, Sec. 4, Roosevelt Road, Taipei 106, Taiwan*
[2]*AHEAD Optoelectronics, Inc., No. 13, Chin-ho Road, Chung-ho, Taipei Hsien 235, Taiwan*

(Received October 14, 1998; accepted for publication November 16, 1998)

The design thinking, implementation, and testing results of a newly developed Doppler interferometer is described. The three built-in measuring modes including (1) single-beam mode for measuring absolute vibration, (2) dual-beam for measuring differential vibration, and (3) distance measuring, are all presented. To facilitate the application of this interferometer for advanced optical storage applications, a circular polarization interferometer configuration was adopted to arrive at a compact size and to enable the adoption of a built-in microscopic imaging system that can be used both as an alignment aid and as a sample imaging system. The configuration of the inherent dynamic system analysis capabilities that can be used to investigate the Bode plot of optical storage systems is also examined in detail. The nanometer resolution and megahertz bandwidth capabilities of this interferometer were verified in various advanced optical storage systems related experiments.

KEYWORDS: Doppler effect, interferomter, vibrometer, optical storage, flying height measurement, flying height modulation, near-field optical recording

## 1. Introduction

The rapid advancement of today's ultra-high performance machinery such as optical/magnetic disk drives, digital video disk drives, etc. has placed ever more stringent demands on metrology tools that can meet a significant portion of these high performance devices.[1–33] With their high accuracy and wide bandwidth, interferometers[8–13,20–26] are natural choices to meet these demanding needs. However, the ever decreasing size of the above mentioned high performance mechanical systems, especially that of today's storage systems, have placed a very strong call for a new breed of interferometers so as to facilitate metrology needs. In addition, to satisfy the rapid advancement and short product cycle time, ease-of-use must be the major consideration in developing a new interferometer. For example, the mechanical alignment stages should become built-in in order to spare users from designing and building mechanical alignment fixtures on their own. Furthermore, the alignment/adjustment stages should be as straightforward and as orthogonal as possible so as to facilitate operations.

In order to design a brand new interferometer system from scratch so as to satisfy the metrology needs of today's storage systems, features of an ideal interferometer must be established as a design guide. After carefully examining the types of metrology applications covering today's higher performance mechanical and mechatronic systems, it is clear that the ideal features needed in the new interferometer include: (1) the possibility of detecting absolute/differential vibration, (2) no special treatments to measurement surfaces, (3) ability to accommodate samples with significantly different reflectivity, (4) nanometer resolutions, and (5) mega-hertz bandwidths.[12] These five design goals served as the design goals for developing the Doppler interferometer described in this article.

*[1]E-mail address: cklee@memsu1.iam.ntu.edu.tw
*[2]E-mail address: james@ahead.com.tw

## 2. Design Implementation

Using the above mentioned design guide as a goal, an advanced vibrometer/interferometer device[12,32,33,38,39] (*AVID*) was designed based on those requirements. Figures 1(a)–1(c) describes the three built-in optical configurations. On the other hand, the physical layout[24,30–33] and the mechanical configurations of *AVID* are shown in Figs. 1(d)–1(e). With all of the alignment stages built-in, *AVID* can convert from a single-beam absolute displacement/velocity metrology instrument shown in Fig. 1(a) to a dual-beam differential displacement/velocity metrology instrument as shown in Fig. 1(b). The conversion requires only a simple pull of the sliding stage, carrying the corner cube in-and-out of the interferometer arm in which light beam 2 propagates. It is also clear from Figures 1(a) and 1(b) that there is no need to create a specular reflective surface on the test surface as each lens projects a point source onto the testing surface. The above discussions indicate that both the first and the second design goals were met. In addition, replacing two focal lenses with two corner cube reflectors transforms *AVID* into a single-frequency distance measurement interferometer (Figure 1c).

The design thinking of *AVID* began with significantly reducing the size of the overall vibrometer/interferometer system including all of the alignment stages that are needed to properly adopt an advanced interferometer to an advanced storage system. To achieve this goal, the circular polarization interferometer configuration was chosen so as to remove the directional ambiguity without resorting to the adoption of an acoustic-optical modulator (AOM) within the small footprint desired and implemented. This design choice reduces the cumbersome and bulky shielding needed to block the RF electromagnetic interference typically associated with an AOM. This circular polarization interferometer configuration can be better understood by tracing the optical path associated with the interferometer herein.

### *2.1 Optical configuration*

The He–Ne laser with better than a 500 to 1 extinction ratio is coupled into the interferometer head with a single-mode

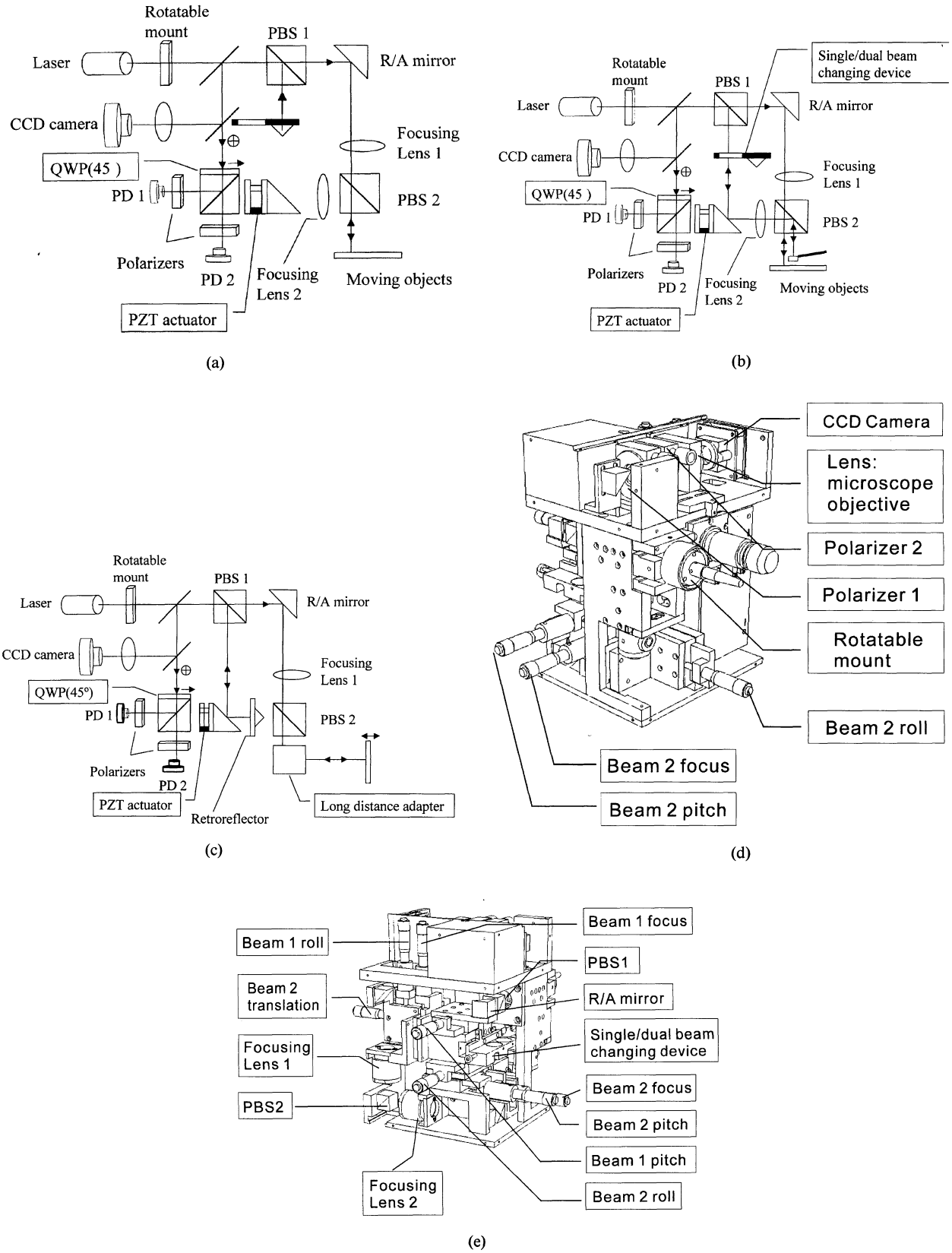


Fig. 1. The measurement modes and mechanical design of AVID. (a) single-beam absolute mode (b) dual-beam differential mode (c) distance measurement mode (d) left view of mechanical configuration (e) right view of mechanical configuration

polarization-preserving optical fiber (Fig. 1), which maintains the polarization state of the incident light beam. The emitting end of the output fiber was mounted on a rotatable mount to adjust the relative intensities of the two outgoing laser beams after it is split by the first polarization beamsplitter (PBS). As a typical PBS can create better than a 100 to 1 extinction ratio, this design provide us with an opportunity to accommodate samples with up to 100 times difference in reflectivity with ease. This range can meet almost all typical metrology conditions. The optimum output beam intensities will then

make the two returning optical beams equal in intensity. This design configuration satisfies the third design goal.

After the laser light was split into two interference arms by the PBS1, light beam 1 passes through beamsplitter PBS2 and focuses onto a point source on the target surface by using focusing lens 1. In addition, light beam 2 passes through a symmetrical path in a differential mode (Fig. 1(b)). In an absolute mode, the internal corner cube (Fig. 1(a)) reflects light beam 2 back to the photodiode to act as the reference light beam. The outgoing laser beam passes through the focusing lens slightly off-axes in order to make the returning light beam be located at different locations of the focusing lens. This off-axes configuration creates the separation needed to differentiate outgoing and returning beams. More specifically, an aperture mirror located behind the PBS1 was used to separate the outgoing and returning light beams. Furthermore, as the two focusing lenses were operated in an off-axis mode, an optical simulation program CodeV[40] was used to select the proper lenses that would have the suitable optical wavefront and acceptable focusing spot. In the end, several sets of doublet lenses were chosen to meet the various application ranges.

The orthogonally polarized states of the two laser beams created by the PBS1 provide us with an opportunity to distinguish beam 1 and beam 2 by using their respective polarization states. More specifically, the PBS2 can be adopted effectively solely because of the two orthogonally polarized light beams. Also, due to the configuration mentioned above, the two focal points can be placed anywhere relative to each other. The total adjustment for these two outgoing light beams in the differential mode is designed to be located within a 4 mm square with the mechanical stages used. This feature is extremely important for ultra-high precision measurements such as the flying height measurement of magnetic heads in hard disk drives, flying height measurement of near-field optical storage devices, dynamic characteristic measurement of optical disk drives, etc.

An aperture mirror mentioned above reflects the two returning beams, which are both linearly polarized and are orthogonal with respect to each other. More specifically, returning beams $E_1$ and $E_2$ can be expressed as[34–37]

$$E_1 = \begin{bmatrix} 1 \\ 0 \end{bmatrix} e^{i2\pi(f_l + f_{d1})t}$$

and

$$E_2 = \begin{bmatrix} 0 \\ 1 \end{bmatrix} e^{i[2\pi(f_l + f_{d2})t + \phi]}, \quad (1)$$

where $f_l$ is the frequency of the incident laser beam, and $f_{d1}$ and $f_{d2}$ are the Doppler frequency due to the specimen motion. When light beam 2 is returned internally, $f_{d2}$ equals zero. After being reflected by the aperture mirror, these two returning light beams transmit through a 45 degrees quarter waveplate denoted QWP(45) and become a right circularly polarized light beam and a left circularly polarized light wave. More specifically, if the amplitude of the two returning light beams are identical, the recombined light beam after QWP(45) can be expressed as:

$$E = \left\{ \begin{bmatrix} 1 \\ i \end{bmatrix} e^{i2\pi f_{d1} t} + \begin{bmatrix} i \\ 1 \end{bmatrix} e^{i(2\pi f_{d2} t + \phi)} \right\} e^{i2\pi f_l t}. \quad (2)$$

Equation (2) clearly shows that the final resultant vector is the vector sum of the two circularly polarized light waves, which can be viewed as a linearly polarized light with its polarization axis located at $[2\pi(f_{d1} - f_{d2})t + \phi]/2$. As the rotatable mount can be used to adjust the relative intensity of the outgoing laser beam, the amplitudes of the two returning light beams can certainly be set to be equal. That is, the recombined light vector is a linearly polarized light beam whose plane of polarization rotates through 360 degrees for a two-wavelength change, which equals to an one-wavelength of relative displacement of the two specimens under test, in the optical path difference between the two light beams.

The 50% non-polarization beam splitter (NPBS) located immediately behind the quarter waveplate then splits the intensity of this re-combined light beam equally. The two polarizers P1 and P2, situated 45 degrees apart, transforms the polarization states into quadrature intensity signals P and Q which can then be detected by photodiodes PD1 and PD2. Since the spatial axes of the two polarization beamsplitters are 45 degrees apart, the P/Q signals detected from PD1 and PD2 are

$$P \propto 1 + B\sin[2\pi(f_{d1} - f_{d2})t + \phi_0]$$

and

$$Q \propto 1 + A\cos[2\pi(f_{d1} - f_{d2})t + \phi_0], \quad (3)$$

where $f_d = f_{d1} - f_{d2}$ is the relative Doppler phase shift created by the moving specimen surfaces and $\phi_0$ is the initial phase. In brief, when the two laser beams are reflected by the two moving targets, the difference of the two Doppler frequency shift $f_d$ becomes

$$f_d = 2V/\lambda = f_l(2V/c), \quad (4)$$

where $f_l$ is the laser frequency, $c$ is the speed of light and $V$ is the relative velocity between the two targets parallel to the laser beam. Since the time dependent phase variation $\phi$ is produced by the relative displacement $D$ between the two targets, the relationship of $\phi$ and $D$ can be shown to be

$$\begin{aligned} \phi/2\pi &= f_l(2D)/c = 2f_l Vt/c \\ &= (f_{d1} - f_{d2})t. \end{aligned} \quad (5)$$

Hence the displacement $D$ can be determined by measuring the phase variation $\phi$. If we perform a standard quadrature signal detection to the above two signals, the relative position between the two object surfaces can be obtained in real time.

In terms of detecting velocity on the circular polarization interferometer configuration adopted in *AVID*, the P/Q signals are mixed with another electronically generated cosine and sine signals of frequency $f_c$ respectively to yield:

*Cosine channel*:

$$\begin{aligned} &A\cos[2\pi(f_{d1} - f_{d2})t + \phi] \cdot \cos(2\pi f_c t) \\ &= \frac{A}{2}\{\cos[2\pi(f_d + f_c)t + \phi] + \cos[2\pi(f_d - f_c)t + \phi] \end{aligned} \quad (6)$$

and

*Sine channel*:

$$- B\sin[2\pi(f_{d1} - f_{d2})t + \phi] \cdot \sin(2\pi f_c t)$$
$$= \frac{B}{2}\{\cos[2\pi(f_d + f_c)t + \phi] - \cos[2\pi(f_d - f_c)t + \phi] \quad (7)$$

Summing these two signals with proper proportional constants yields an output signal of $\cos[2\pi(f_d + f_c)t + \phi]$. Sending this signal into a simple frequency-to-voltage converter yields a velocity signal due to the Doppler effect. Thus *AVID* can measure both velocity and displacement independently by performing frequency demodulation and phase decoding respectively.

### 2.2 *Signal processing algorithm and self-calibration*

Sending the two signals shown in eq. (3) through the pre- and post-amplifier yields the P/Q signals as shown in Fig. 2. It is clear from eq. (3) that sending these quadrature signals into the horizontal and vertical input of an oscilloscope, a Lissajous circular pattern can be obtained. If the P/Q signals are ideal, the Lissajous circular pattern should be a full circle similar to the one shown in Fig. 3. Despite all the design considerations, the two returning beams may not have identical amplitude and the phase difference may not be exactly 90 degrees in real experimental conditions due to noise. The typical Lissajous circular pattern will thus appear to be elliptical in shape (Fig. 4). As one full circle on the Lissajous circle corresponds to a 360 degrees relative displacement between the two beams, each degree of the phase angle then corresponds to approximately 0.88 nm (=632.8 nm/2/360) of relative displacement. It is also clear from the above analysis that to meet the fifth design goal which demands nanometer resolution and mega-Hertz response, the Lissajous circular pattern must be decoded to 1 degree or so.

The major drawback in the decoding phase from the elliptical pattern similar to the one shown in Fig. 4 is that the same amount of the elliptical boundary path corresponds to more swept angles near the long axis when compared to that of the short axis. This is equivalent to saying that a twisted Lissajous circular pattern will have a different resolution when the signal is decoded near the long axis versus that of the short axis. This effect is typically neglected by the more traditional interferometers. An algorithm that corrects this drawback was developed during the development of this new interferometer. This new algorithm circumvents the unequal accuracy problem by transforming the ellipse to a corresponding normalized circle. The fundamental thinking is that a user really cannot discern the signal from the noise when the noise induced error is traversed along the Lissajous circle. A least square method was thus used to identify an ellipse that has to minimize the difference between every point and of the ellipse along the radial direction. Once the ellipse is identified, the associated elliptical parameters were used to transform the twisted Lissajous elliptical pattern into a normalized Lissajous circular pattern.

To decode the Lissajous circle to such a large number of sub-divisions, a high-speed PC-based analog-to-digital (A/D) card was used to perform the digital processing of the quadrature signal. Using a simple 250 MHz analog-to-digital (A/D) card to digitize the quadrature signal gives *AVID* a bandwidth of at least 20 MHz, which is almost 50 times higher than most commercially available interferometers. Considering the case of near-field optical recording, the full measurement range of the displacement can be less than 316.4 nm, a new calibration scheme must be developed to minimize errors generated from the incomplete identification of the elliptical parameter for the Lissajous pattern. A built-in piezoelectric stack actuator was thus incorporated in the path of light beam 2 to create optical path difference (OPD) at least corresponds to a full Lissajous circle after the two light beams were aligned. By capturing this PZT actuator induced Lissajous circle, the required elliptical parameters can be retrieved. Once the normalization is accomplished, the phase angle of the Lissajous circle can certainly be accurately determined.

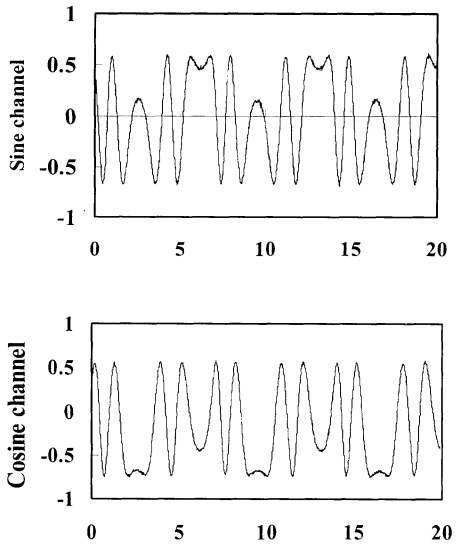


Fig. 2. Quadrature signals P and Q from *AVID*.

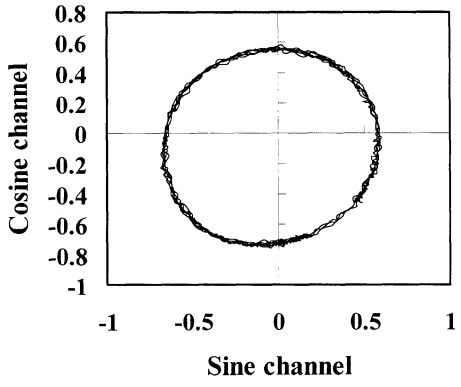


Fig. 3. Circular Lissajous pattern from ideal quadrature signals.

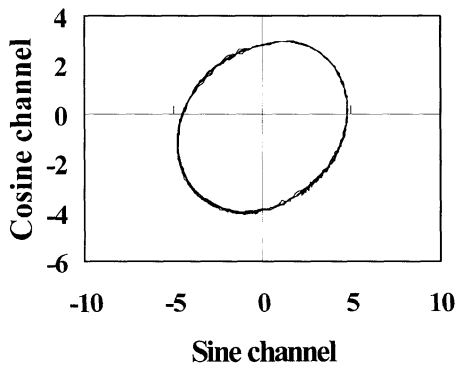


Fig. 4. Typical elliptical Lissajous pattern from *AVID*.

From Fig. 5, it is clear that $A_P$ and $A_q$ are the amplitudes, $\alpha$ and $\beta$ represent the phase of the P/Q signal, respectively, and denotes the phase angle of the initial point (reference point) on the Lissajous graph. The coordinate of an arbitrary point on the ellipse can be expressed by the following matrix equations:

$$\begin{bmatrix} x \\ y \end{bmatrix} = \begin{bmatrix} R_A \cos(\theta + \varepsilon) \\ R_B \sin(\theta + \varepsilon) \end{bmatrix}, \tag{8}$$

$$\begin{bmatrix} q \\ p \end{bmatrix} = \begin{bmatrix} \cos\delta & -\sin\delta \\ \sin\delta & \cos\delta \end{bmatrix} \begin{bmatrix} x \\ y \end{bmatrix} + \begin{bmatrix} B_q \\ B_p \end{bmatrix}, \tag{9}$$

$$\begin{bmatrix} A_q \sin(\theta + \alpha) \\ A_p \sin(\theta + \beta) \end{bmatrix} = \begin{bmatrix} A_q \sin\theta\cos\alpha + A_q \cos\theta \sin\alpha \\ A_p \sin\theta\cos\alpha + A_p \cos\theta \sin\alpha \end{bmatrix} = \begin{bmatrix} q - B_q \\ p - B_p \end{bmatrix}, \tag{10}$$

and

$$\begin{bmatrix} q - B_q \\ p - B_p \end{bmatrix} = \begin{bmatrix} (R_A \cos\varepsilon\cos\delta - R_B \sin\varepsilon\sin\delta)\cos\theta - (R_A \sin\varepsilon\cos\delta + R_B \cos\varepsilon\sin\delta)\sin\theta \\ (R_A \cos\varepsilon\sin\delta + R_B \sin\varepsilon\cos\delta)\cos\theta - (R_A \sin\varepsilon\sin\delta - R_B \cos\varepsilon\cos\delta)\sin\theta \end{bmatrix}. \tag{11}$$

Simplifying eqs. (8)–(11) yields

$$A_p{}^2 = R_A{}^2 \sin^2\delta + R_B{}^2 \cos^2\delta, \tag{12}$$

$$A_q{}^2 = R_A{}^2 \cos^2\delta + R_B{}^2 \sin^2\delta, \tag{13}$$

and

$$A_p A_q \cos(\alpha - \beta) = (R_A{}^2 - R_B{}^2)\sin\delta\cos\delta, \tag{14}$$

where $\alpha$, $\beta$ can be replaced by the phase difference$(\alpha - \beta)$. Now, the three parameters $A_p$, $A_q$, and $(\alpha - \beta)$ are functions of $R_A$, $R_B$, and $\delta$. They are independent of the value $\varepsilon$, phase angle of the reference point. This fact holds whether the measurement point is on the circle or on the ellipse. Next, we assume angle $\beta = 0$ as a reference point. Its coordinates can be expressed as

$$\begin{bmatrix} p \\ q \end{bmatrix} = \begin{bmatrix} B_p + A_p \sin\theta \\ B_q + A_q \sin\alpha\cos\theta + A_q \cos\alpha\sin\theta \end{bmatrix}. \tag{15}$$

As eq. (15) contains many nonlinear components, matrix operations cannot be applied. Therefore, to overcome this problem, some mappings were adopted to linearize the equations. That is, choosing

$$C_q = A_q \sin\alpha, \quad \text{and} \quad D_q = A_q \cos\alpha, \tag{16}$$

then

$$\begin{bmatrix} p - B_p \\ q - B_q \end{bmatrix} = \begin{bmatrix} 0 & A_p \\ C_q & D_q \end{bmatrix} \begin{bmatrix} \cos\theta \\ \sin\theta \end{bmatrix}. \tag{17}$$

For the convenience of calculations, an inverse matrix $\begin{bmatrix} 0 & A_p \\ C_q & D_q \end{bmatrix}^{-1} = \begin{bmatrix} \overline{C_p} & \overline{D_p} \\ \overline{C_q} & 0 \end{bmatrix}$ was used during the computations of $\begin{bmatrix} \cos\theta \\ \sin\theta \end{bmatrix}$. Therefore,

$$\begin{bmatrix} \cos\theta \\ \sin\theta \end{bmatrix} = \begin{bmatrix} \overline{C_p} & \overline{D_p} \\ \overline{C_q} & 0 \end{bmatrix} \begin{bmatrix} p - B_p \\ q - B_q \end{bmatrix} = \begin{bmatrix} \overline{C_p} & \overline{D_p} & \overline{B_p} \\ \overline{C_q} & 0 & \overline{B_q} \end{bmatrix} \begin{bmatrix} p \\ q \\ 1 \end{bmatrix}, \tag{18}$$

where $\begin{bmatrix} \overline{B_p} \\ \overline{B_q} \end{bmatrix} = \begin{bmatrix} \overline{C_p} & \overline{D_p} \\ \overline{C_q} & 0 \end{bmatrix} \begin{bmatrix} -B_p \\ -B_q \end{bmatrix}$.

These five terms $\overline{C_p}$, $\overline{C_q}$, $\overline{D_p}$, $\overline{B_q}$, and $\overline{B_q}$ can map the ellipse to a normalized circle. Thus, we can easily use them rather than $A_p$, $A_q$, $B_p$, $B_q$, and $(\alpha - \beta)$ to identify the characteristics of the signals obtained. As was mentioned above, the physical meaning of the P/Q signal suggests that radial noises result in a little error between the specific sampled data and its corresponding point on the ellipse. Defining radial error as the radial distance between the measured data points and its corresponding point on the ellipse which depend on the five parameters $\overline{C_p}$, $\overline{C_q}$, $\overline{D_p}$, $\overline{B_p}$ and $\overline{B_q}$, yields

$$e_i = 1 - \begin{bmatrix} \cos\theta_i \\ \sin\theta_i \end{bmatrix}^T \begin{bmatrix} p_i & q_i & 1 & 0 & 0 \\ 0 & 0 & 0 & p_i & 1 \end{bmatrix} \begin{bmatrix} \overline{C_p} \\ \overline{D_p} \\ \overline{B_p} \\ \overline{C_q} \\ \overline{B_q} \end{bmatrix}. \tag{19}$$

Next, minimizing the sum of errors is required to achieve the best fitting curve. We can consider each $e_i$ term as a radial error vector in a $N$-dimensional space where $N$ is the number of data points which identify the corresponding phase angle. The least square method demands that all of the five partial derivatives of $F = \sum_{i=1}^{N} e_1{}^2/N$ with respect to $\overline{C_p}$, $\overline{C_q}$, $\overline{D_p}$, $\overline{B_p}$, and $\overline{B_q}$ equal

to zero such that

$$\begin{bmatrix} \overline{C_p} \\ \overline{D_p} \\ \overline{B_p} \\ \overline{C_q} \\ \overline{B_q} \end{bmatrix} = \left( \sum_{i=1}^{N} \begin{bmatrix} p_i \cos\theta_i \\ q_i \cos\theta_i \\ \cos\theta_i \\ P_i \sin\theta_i \\ \sin\theta_i \end{bmatrix} \begin{bmatrix} \cos\theta_i \\ \sin\theta_i \end{bmatrix}^T \begin{bmatrix} P_i & q_i & 1 & 0 & 0 \\ 0 & 0 & 0 & p_i & 1 \end{bmatrix} \right)^{-1} \left( \sum_{i=1}^{N} \begin{bmatrix} p_i \cos\theta_i \\ q_i \cos\theta_i \\ \cos\theta_i \\ p_i \sin\theta_i \\ \sin\theta_i \end{bmatrix} \right). \quad (20)$$

Equation (20) allows us to identify $\overline{C_p}$, $\overline{C_q}$, $\overline{D_p}$, $\overline{B_q}$, and $\overline{B_q}$ provided that we know $p_i$, $q_i$, $\cos\theta_i$, and $\sin\theta_i$ for every sampled point. The detailed operating procedures are described herein.

Firstly, two arrays of P/Q signals, ($p_i$, $q_i$), generated by exerting externally applied voltage to the built-in piezoelectric stack actuator with the sample in place was recorded to determine the elliptical parameters, $\overline{C_p}$, $\overline{C_q}$, $\overline{D_p}$, $\overline{B_p}$, and $\overline{B_q}$. Secondly, $\cos\theta_i$ and $\sin\theta_i$ was determined by the recorded ($p_i$, $q_i$) value. From the theory described earlier, it is clear that the initial identification of the biased value does not significantly influence the numerical result since the true biased value will be determined by iterations later on. Thus $B_p$ and $B_q$ can be determined as if the Lissajous pattern is ideal, i.e.,

$$B_p = \frac{1}{2}(\max(p_i) + \min(p_i))$$

and

$$B_q = \frac{1}{2}(\max(q_i) + \min(q_i)) \quad (21)$$

The initial phase angle $\theta_i$ can then be estimated as

$$\theta_i = \tan^{-1}((p_i - B_p)/(q_i - B_q)). \quad (22)$$

Thirdly, all the $p_i$, $q_i$, $\cos\theta_i$ and $\sin\theta_i$ values were substituted into eq. (20) to compute the five parameters $\overline{C_p}$, $\overline{C_q}$, $\overline{D_p}$, $\overline{B_p}$, and $\overline{B_q}$. As the original $B_p$ and $B_q$ are not free of errors, it is necessary to perform iterations to approach the best fit values. Before iterations were performed, $\cos\theta_i$ and $\sin\theta_i$ were normalized to make sure the sum of the square equaled to 1. i.e.

$$\begin{bmatrix} \cos\theta_i \\ \sin\theta_i \end{bmatrix} = \frac{\begin{bmatrix} \overline{C_p} & \overline{D_p} & \overline{B_p} \\ \overline{C_q} & 0 & \overline{B_q} \end{bmatrix} \begin{bmatrix} p \\ q \\ 1 \end{bmatrix}}{\left\| \begin{bmatrix} \overline{C_p} & \overline{D_p} & \overline{B_p} \\ \overline{C_q} & 0 & \overline{B_q} \end{bmatrix} \begin{bmatrix} p \\ q \\ 1 \end{bmatrix} \right\|}. \quad (23)$$

The $\cos\theta_i$ and $\sin\theta_i$ obtained from eq. (23) were substituted into eq. (20) to perform iterations until the resultant $\cos\theta_i$ and $\sin\theta_i$ pairs converged. Once the $\cos\theta_i$ and $\sin\theta_i$ values are converged, eq. (20) was used to compute the five elliptical parameters. Next, substituting $\overline{C_p}$, $\overline{C_q}$, $\overline{D_p}$, $\overline{B_p}$ and $\overline{E_q}$ into eq. (18) first and then into eq. (23) allows us to arrive at the most accurate $\cos\theta_i$ and $\sin\theta_i$ pairs. Once the accurate $\cos\theta_i$ and $\sin\theta_i$ pairs are obtained, the corrected phase angle can be retrieved by taking an arc-tangent function. The displacement $D$ and the phase angle can be related by eq. (5).

It is with the above-mentioned built-in PZT calibration actuator design and the newly developed phase angle retrieving algorithm that *AVID* was able to meet our fifth design goal.

### 2.3 *Alignment steps and built-in microscopic imaging system*

It should be noted that the easy conversion from the absolute mode to the differential mode is not only a novelty but also part of the alignment/setup procedures designed. This design thinking facilitates the possibility of integrating the two configurations shown in Figs. 1(a)–1(c) into a very compact package approximately 14 cm on every side for the optical head as shown in Figs. 1(d) and 1(e). The compact yet balanced mechanical design shown in these figures naturally creates the structural thermal stability needed for high precision interferometry measurements. As all of the built-in alignment stages are designed to have the optical alignment action orthogonal to each other, adjusting the yaw and pitch angles of light beam 1 can be achieved by two stages. More specifically, it is one of the basic *AVID* design thinking that the adjustment of any stage will handle only one optical alignment functions. Considering that *AVID* has a maximum of two object beams and each beam must be able to perform focusing, one axis of translation, and handle two angular orientations of the sample surface, i.e. the pitch and the yaw, a minimum of four stages are needed to arrive this design goal. In addition, the translation of the two beams must be orthogonal in order to maximize the measurement area that can be covered by the two object light beams. The measurement range is determined by the maximum translation ranges of the built-in stages. In our current implementation, the measurement area is 4 mm by 4 mm. Furthermore, the maximum pitch and yaw angles of the sample surface that can be compensated by the built-in stages are determined by the focal length of focusing lenses 1 and 2, which is approximately 2 degrees maximum for lenses with a current 60 mm focal length. To further facilitate the alignment efforts for measuring storage systems that are typically of many different mechanical configurations, an external fixture that has the capability to adjust the up and down movements, the tilting, and the rotation of the whole

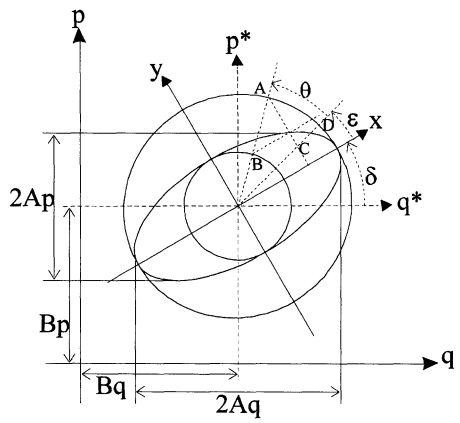


Fig. 5. Elliptical parameters of a general quadrature signal.

optical head was also designed (Figs. 6 and 7). Figures 6 and 7 demonstrate the relative orientations between *AVID*, the external fixture, and a storage system under test.

As an AOM is not used in *AVID*, the interference fringes generated is thus observable as it will not move at the AOM frequency which is typically 40 MHz. This characteristic provides us with an opportunity to create an internal interference fringe observing optics so as to guide the alignment direction. It can be seen from Fig. 1 that approximately 8% of the two returning light beams $E_1$ and $E_2$ (eq. (1)) were extracted by the NPBS located behind the aperture mirror. This 8% light beam is then sent through the built-in light beam imaging system that consists of two polarizers, a microscope objective lens and a CCD camera. The first polarizer acts as the analyzer that makes $E_1$ and $E_2$ interfere as those two laser beams are orthogonally polarized. As the laser beam becomes linearly polarized after the first polarizer, the second polarizer then acts like an attenuator to make sure the interference fringes generated are located within the dynamic range of the CCD. The microscope object lens can be moved forward and backward so as to make the built-in light beam image system acts like an auto-collimator or as an alignment telescope in order to facilitate rapid sample alignment/focusing and measurement location identification.

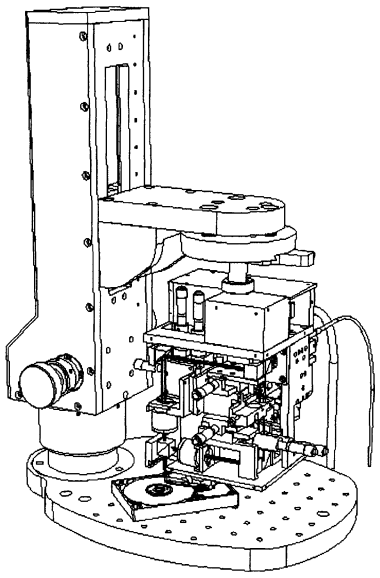

Fig. 6. Coupling alignment fixures and samples.

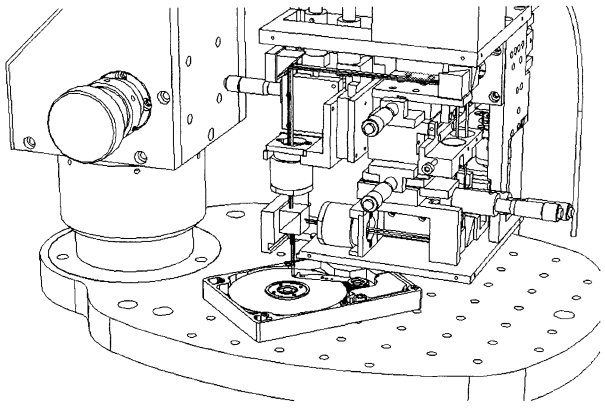

Fig. 7. Close-up view of *AVID* and samples.

More specifically, as the interference fringes between the two interferometry-arms are observable, a new set of alignment and sample imaging procedures can be developed to facilitate the setup of an interferometer. The alignment operation of *AVID* is described below. When *AVID* is first turned on, it is typically put in the single-beam absolute mode. In addition, the focal point of the microscope objective is placed at the image plane of the CCD camera. In other words, two parallel incident light beams will appear as one spot on the CCD. In this configuration, the image observed through the CCD camera (Fig. 1) and captured by the frame grabber located within the PC is shown in Fig. 8(a). The image of light beam 2 that is reflected by the built-in corner cube will appear in the screen as the alignment reference. The light beam 1 image will appear as a second spot on the screen indicting that the two light beams are not parallel to each other. Since the alignment stages were designed to have orthogonal optical alignment functions, the effect of the light beam 1 pitch and yaw angular adjustments can be observed as two translations on the screen. In addition, the focusing action of beam 1 can be achieved by making sure the interference fringes have a minimum number of concentric fringes. If the sample surface has a reasonable optical quality, the interference fringe induced by $E_1$ and $E_2$ will appear as a spot that blinks full black and then full bright when the built-in piezoelectric translation stage is driven by a low frequency voltage signal. Fine tuning of light beam 1 can be achieved by observing the relative orientations and locations of the two returning light beams by placing the microscope objective in various locations which makes the light beam image optics act like an alignment telescope. If *AVID* is to be operated in the differential mode, light beam 1 that is aligned in the absolute mode will then serve as the reference beam. Similar adjustments can then be done to align light beam 1.

As the microscope object lens of the light beam image optics is confocal with respect to focusing lenses 1 and 2, the sample surface(s) will be in focus once *AVID* is aligned. Introducing appropriate external lighting, the location of the measurement spots and the sample image will appear in the screen simultaneously as shown in Fig. 8(b). Since the magnification factor $M$ of the sample image on the screen can be determined as

$$M = (l_m/l_o)M_c, \tag{24}$$

where $l_m$ and $l_o$ represents the focal length of the microscope objective and focusing lens respectively, and $M_c$ is the magnification factor created by the CCD and screen, the value $M$ can be determined *a priori* and will remain identical as long as the factors listed in eq. (24) remain unchanged. This feature provides us with an opportunity to determine the measurement locations precisely. In addition, the sample surfaces can be observed if external lightning is introduced. The above-mentioned discussions further demonstrate the level of integration and show how a circular polarization interferometry configuration can be extended to facilitate advanced mechanical systems metrology.

## 3. Experimental Set-up

Several experiments were performed to examine the capability, measurement accuracy, and level of integration men-

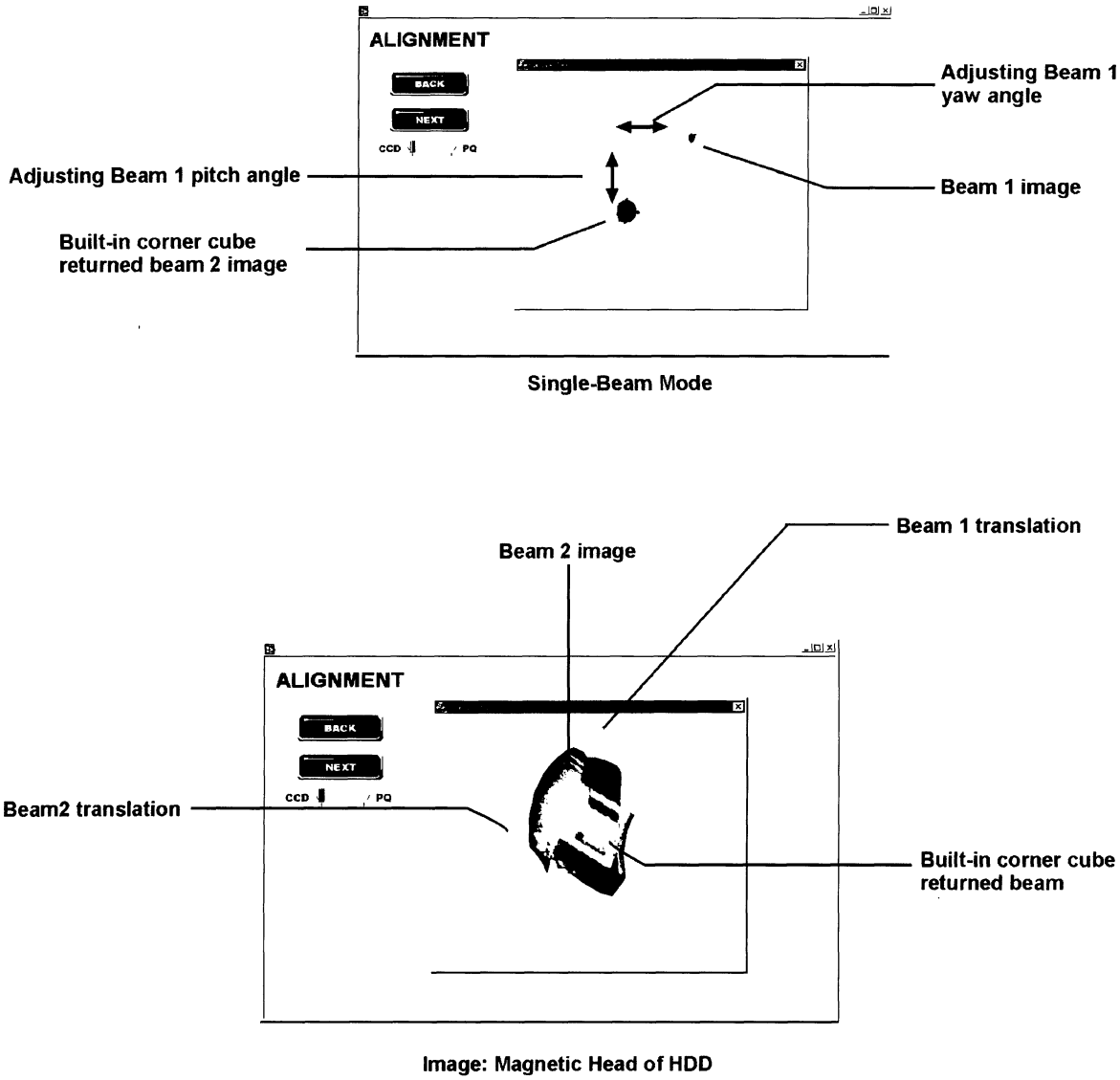


Fig. 8. Visual aid of *AVID* alignment (a) and sample imaging (b).

tioned above. Items discussed include runout measurement of high precision spindles, slider flying height measurements, slider flying height modulations, and transfer functions of focusing and tracking of DVD optical pick-up heads, etc.

### *3.1 Runout and vibration analysis of optical storage devices*

For instance, total indicated runout (TIR) or runout of the spindle and bearing are traditionally measured by placing a proximity transducer adjacent to the measured point of the spindle. The TIR signals can then be recorded on a storage oscilloscope. Taking the average of several traces by aligning each signal with respect to a common timing mark such as the index pulse gives us the averaged runout called repeatable runout (RRO). Subtracting repeatable runout from any single trace of data yields to a non-repeatable runout (NRRO). The NRRO gives a clear indication of the spindle quality. With the ever more stringent demands of volume density requirements for storage devices such as optical or magnetic files, disk spacing has been driven to a much smaller value. To characterize continuously evolving disk files, a system with better accuracy than that of the proximity sensor is needed. In addition, the trend of moving towards thinner disks also makes accurate placement of the transducer more important. The runout data shown in Figs. 9(a) and 9(b) are TIR, RRO and NRRO measured at the inner diameter (ID) of an experimental optical disk. It can be seen from the data that RRO and NRRO are approximately 22 $\mu$m and 5 $\mu$m peak-to-peak respectively. The results clearly demonstrate that *AVID* is capable of handling the challenges mentioned above.

### *3.2 Spacing and flying height modulation measurements*

To examine the nanometer resolution and accuracy achievable by *AVID* in studying advanced storage systems, data obtained from *AVID* was compared to analog magnetic readback signals from magnetic disk drives. Successful demonstration of this comparison indicates that *AVID* is applicable for evaluating the performance of today's near-field optical recording technologies.

Considering Wallace spacing loss,[41] the analog magnetic readback signal $V(t, z)$ obtained by flying a magnetic head over a pre-written periodical magnetic track signal of frequency $f$, wavelength $\lambda$, and flying height $z$ can be shown to be[42,43]

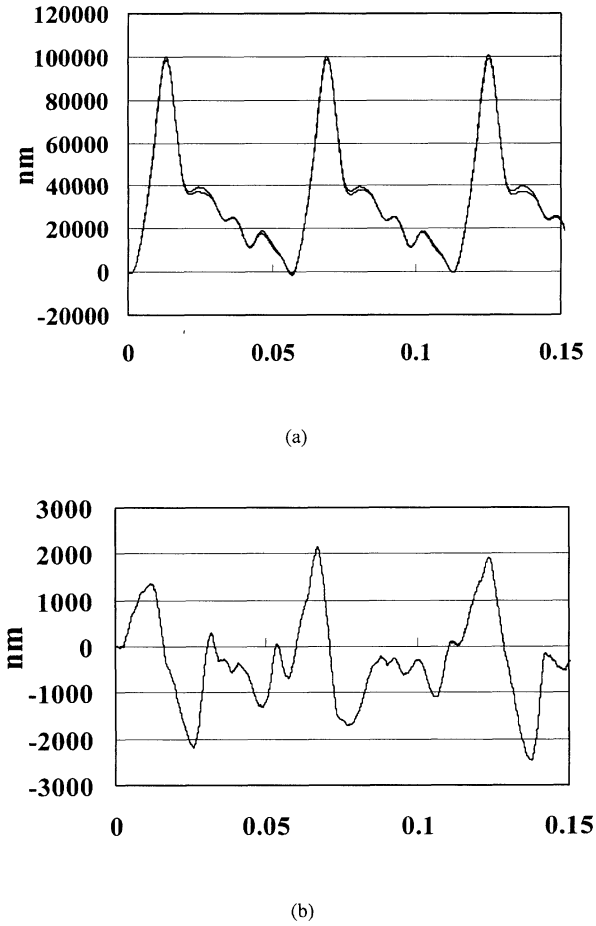


Fig. 9. Runout of optical disk (a) RRO and TIR mode (b) NRRO mode.

$$V(t, z) = CV(t, 0)e^{-kz}, \tag{25}$$

where $C$ is a constant and a function of the magnetic head, $V(t, 0)$ is the analog readback signal at zero flying height, and $k = 2\pi/\lambda$ is the wave-number of the magnetic signal. Assuming that the frequency response of the recording channel is flat over all frequency bands and the magnetic head is linear with respect to the magnetic signal amplitude during a spin-down, the spacing loss $\Delta z$ of the magnetic head can be derived from eq. (25) to be

$$\Delta z = -[20 \log V(t, z)/V(t, 0)]\lambda/(2\pi \log e), \tag{26}$$

where $[20 \log V(t, z)/V(t, 0)]$ is the analog readback signal represented in $dB$. The magnetic spacing of the flying head can then be calculated according to eq. (26) once the magnetic head is calibrated.

Operating *AVID* in the differential mode is done by placing light beam 1 on the back of the flying slider and the light beam 2 on a disk location that is adjacent to light beam 1. Assuming that the slider is a rigid body and that the flying height is a function of the disk velocity only, the spacing at the pole-tip location can be derived by performing three measurements on three non-collinear locations of the back of the slider.[12] As *AVID* is equipped with built-in image optics, the three measurement locations performed can be retrieved accurately, the only difficulty may lie in the fact that *AVID* has no way of determining the instant that the slider is lift off the disk. That is, the origin of the spacing measurement, i.e., the point where the slider lifts off the disk, cannot be determined by using *AVID* alone. This task is achieved by incorporating a piezoelectric transducer made from PZT (lead, zirconate, titanate) that is mounted at the end of the actuator where the slider is attached.[12,44–46] Once the slider is lifted off the disk, the PZT signal will then suddenly drop to its lowest point as can be seen in Fig. 10. Figure 10 compares the flying height data obtained by *AVID* to that of an analog magnetic readback signal with $\lambda$ equaling 0.72 $\mu$m. It is clear from the data that the flying height data obtained by the two methods are within the flatness specifications of the head calibration instrument. As the difference is less than 1nm, the data also implicitly reflects the resolution and accuracy of *AVID*. The experimental results shown in Fig. 10 strongly demonstrates that *AVID* can be applied to measure the spacing of today's near-field optical storage systems.

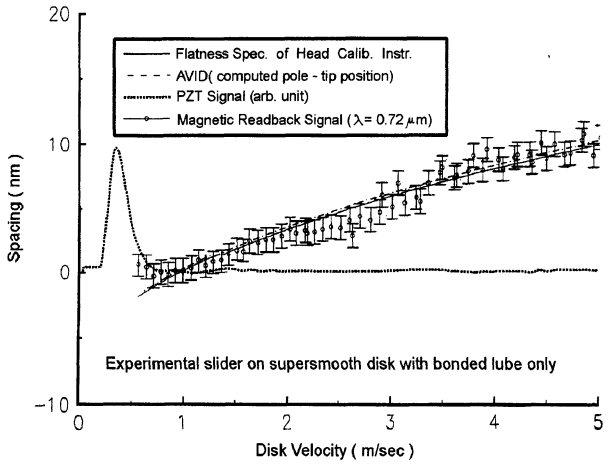


Fig. 10. Comparison of spacing measurements by magnetic readback signal and *AVID*.

Another data that is of interest for advanced near-field optical storage systems is the spacing fluctuation of the head carrying sliders at constant disk linear velocity. This can be easily investigated by operating *AVID* in a differential mode similar to the configuration mentioned above for flying height measurements. The data obtained is shown in Fig. 11. To verify the accuracy of this data, analog readback signals were performed twice by using two wavelengths, 1.0 and 0.5 $\mu$m, respectively. The voltage signals obtained were then substituted into eq. (26) to arrive at the spacing fluctuation needed. It is clear from Fig. 11 that the discrepancies among these three measurements are less than 0.5 nm.

Since *AVID* and the analog magnetic readback signal are derived from the spacing data by using completely different physical principles, the experimental results shown in Figs. 10 and 11 strongly demonstrate the applicability, accuracy, and resolution in adopting *AVID* to evaluating the performance of advanced storage systems.

### *3.3 Dynamic analysis of pickup heads for DVDs*

The dynamic characteristics of a DVD pickup head were examined by using *AVID*. To create the Bode plot needed to characterize the pickup head, a system called a Dynamic-Signal-Analyzer (DSA) was developed and integrated into *AVID* to become *AVID-DSA* (Fig. 12). Swept sine measurements was performed to evaluate the performance of a DVD

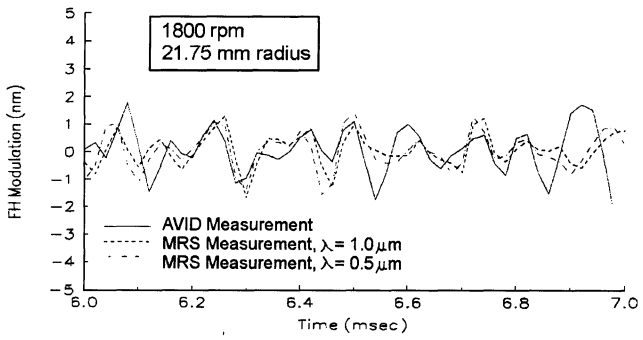


Fig. 11. Comparison of spacing modulation by magnetic readback signal and *AVID*.

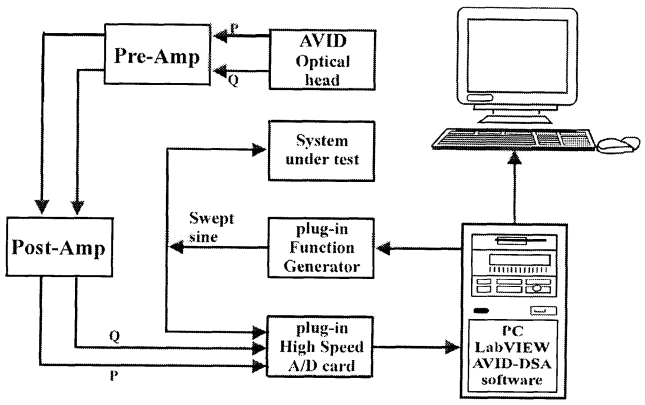


Fig. 12. Block diagram of *AVID-DSA*.

pickup head. The transfer functions that detail the focusing action (Fig. 13(a)) and tracking action (Fig. 13(b)) of a DVD pickup head were obtained by using the single-beam absolute vibration mode of *AVID*. Operating *AVID* in its dual-beam differential vibration mode and placing both measurement beams on top of the focusing lens of a DVD pickup head (Fig. 14) yields the transfer function that represents the rotation motion of the lens during pickup head focusing (Fig. 15). One thing that should be noted is that the experimental data shown in Figs. 13 and 15 were obtained directly on a DVD pickup head without coating any reflective materials on top of the lens. The experimental data shown in Figs. 13 and 15 clearly demonstrate the effectiveness of *AVID-DSA* and that *AVID* indeed meets its original design goals.

### *3.4 Ultrasonic surface wave measurements*

To verify if the mega-Hertz bandwidth design goal of *AVID* is achieved, *AVID* was tested in an application of laser ultrasound with the help of a leading ultrasonic research group at National Taiwan University.[47,48] Longitudinal surface ultrasonic waves generated by pulsing a Nd-YAG laser to a thin optical disk were detected by using *AVID* (Fig. 16). The distance between the pulse laser input location and that of *AVID* was 5.1 cm. The sampling rate of *AVID* was operated at 5 MHz and a total of 2048 data points were measured. It is clear that the first half of Fig. 16 represents symmetric mode oscillations and the later half of Fig. 16 represents an anti-symmetric mode. It is thus possible to take the data shown in Fig. 16 to perform inverse calculations to arrive at Young's

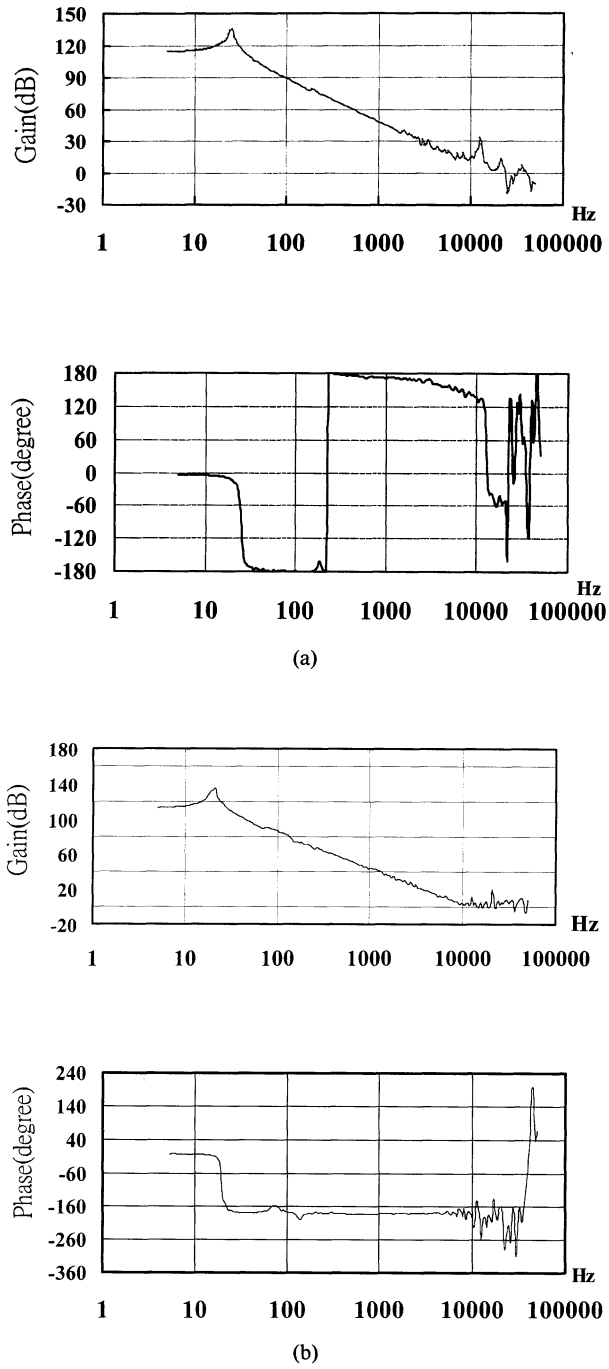


Fig. 13. Focusing transfer function of a DVD pickup head while performing focusing motion. (a), and tracking transfer function of a DVD pickup head while performing focusing motion (b).

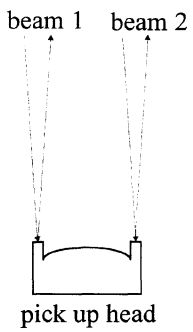


Fig. 14. Laser beam locations for measuring rotational motion of a DVD pickup head.

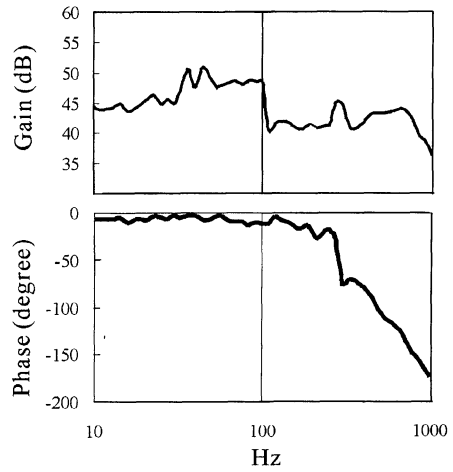


Fig. 15. Rotation transfer function of a DVD pickup head while performing focusing motion.

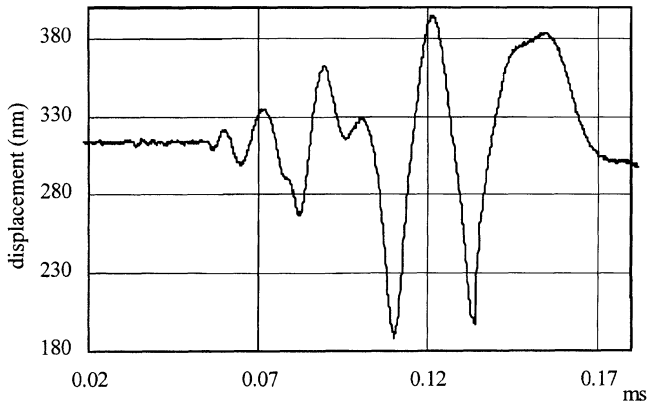


Fig. 16. Experimental data for laser induced ultrasound on an optical disk.

modulus, and shear modulus, etc., of the material of interest. As the longitudinal surface ultrasonic waves have a frequency in the range of a few mega-Hertz, the experimental data shown in Fig. 16 clearly validates the mega-Hertz capability of *AVID*. The system has since been used equally successful in measuring laser ultrasound in metal and non-metal thin plates.

## 4. Conclusions

It is clear from the experimental data obtained that the newly developed Doppler interferometer *AVID* can satisfy the stringent demands of today's ultra-high performance machinery such as optical/magnetic disk drives, compact disk drives, digital video disk drives, micro sensors/actuators, etc. Compared with traditional optical metrology instruments, this interferometer possesses features such as (1) requiring no modifications to measurement surfaces, (2) having an absolute/differential detection capability, (3) is capable of measuring linear and angular displacement and velocity of a structure, (4) is able to accommodate samples with significantly different reflectivities, (5) possesses nanometer resolutions, and (6) has a mega-hertz bandwidth. Thus, this newly developed interferometer, the *AVID* system is well suited to examine the dynamic and static behavior of ultra-high precision high-performance systems.

## Acknowledgements

This research was supported partially by the National Science Council, Taiwan, Republic of China under contract numbers NSC 85-2622-E-002-017R, NSC 86-2622-E-002-023R, and NSC 88-2622-E-002-001.

1) J. M. Harker, D. W. Brade, R. E. Pattision, G. R. Santana and L. G. Taft: IBM J. Res. Develop. **25** (1981) 677.
2) G. R. Briggs and P. G. Herkart: Proc. 1971 Intermag Conf. Denver, Colorado, 1971, p. 418.
3) K. Ono, K. Kagure and Y. Mitsuya: Bull. JSME **22** (1979) 1622.
4) S. E. Millman, R. F. Hoyt, D. E. Horne and B. Beye: IEEE Trans. Mag. MAG-**22** (1986) 1031.
5) R. Sonnenfeld: 1992 Digest of Intermag Conf. St., Louis, Missouri, 1992, Paper No. DB-08.
6) C. Lin and R. F. Sullivan: IBM J. Res. Develop. (1972) 269.
7) D. K. Miu and D. B. Bogy: ASME J. Tribology **108** (1986) 584.
8) A. Nigam: ASME J. Lubrication Technol. **104** (Jan. 1984) 60.
9) G. L. Best, D. E. Horne, A. Chiou and H. Sussner: Trans. Magn. MAG-**22** (1986) 1017.
10) T. Ohkubo and J. Kishigami: Proc. ASLE/ASME Tribology Conf. San Antonio, 1987, ASME Paper No. 87-Trib-28.
11) M. H. Wahl, J. C. Briggs and F. E. Talke: 1992 Dig. of Intermag Conf., St. Louis, 1992, Paper No. DB-10.
12) C. K. Lee and T. W. Wu: AIAA J. **33** (1995) 1675.
13) T. A. Riener, A. C. Goding and F. E. Talke: IEEE Trans. Magn. **24** (1988) 2745.
14) AHEAD Optoelectronics, Inc., B1, No. 130, Sec. 3, Keelung Road, Taipei 106, Taiwan.
15) Polytec Optronics, Inc., 3001 Redhill Avenue, Suite 102, Costa Mesa, CA 92626.
16) Dantec Electronics, Inc., 777 Corporate Drive, Mahwah, NJ 07430.
17) TSI, Inc., 500 Cardigan Road, P. O. Box 64394, St. Paul, MN 55164.
18) Ometron, Inc., 44873 Falcon Place, Suite 118, Sterling, VA 22170.
19) R. Davidson: U.S. Patent No. 4,681,447 (1987).
20) D. Henze, P. Mui, G. Clifford and R. Davidson: IEEE Trans. Magn. **25** (1989) 3710.
21) L. Y. Zhu: Ph.D. Dissertation, Univ. of California, Berkeley, 1988.
22) L. Y. Zhu and D. B. Bogy: STLE Tribology and Mechanics of Magnetic Storage Systems, (1989) No. SP-26, 160.
23) M. Suk, T. Ishii and D. B. Bogy: IEEE Trans. Magn. MAG-**27** (1991).
24) C. K. Lee, C. Y. Wu, G. T. Pan, S. R. Chiang and J. Wu: Tech. Dig. Sum. Int. Symp. Polarization Anal. and Applications to Device Tech. Yokohama, 1996, p. 74.
25) L. Crawforth, C. K. Lee and A. C. Munce: Proc. 1990 Int. Conf on Hologram Interferometry and Speckle Metrology (1990) p. 404.
26) D. Rugar, H. J. Mamin, R. Erlandsson, J. E. Stern and B. D. Terris: Rev. Sci. Instrum. **59** (1988) 2337.
27) G. E. Sommargren: Proc. SPIE 1989 Symp. Microlithography, San Jose, California, 1989.
28) H. C. Lefevre: Electron. Lett. **16** (1980) 778.
29) F. Durst, A. Melling and J. H. Whitelaw: *Principles and Practice of Laser-Doppler Anemometry* (Academic Press, New York, 1981) 2nd ed.
30) C. K. Lee and T. W. Wu: IBM Tech. Discl. Bull. **35** (1992) 189.
31) C. K. Lee, W. W. Chiang, D. W. Meyer, U. V. Nayak, T. C. O'Sullivan and T. W. Wu: IBM Tech. Discl. Bull. **37** (1994) 185.
32) C. K. Lee, C. T. Lin, C. T. Teng, and G. Y. Wu: *Proc. 8th Int. Conf. Adaptive Struct.* (Technomic Publishing, Lancaster, Pennsylvania, 1997) p. 166.
33) C. K. Lee, G. Y. Wu, W. J. Wu, K. S. Yeh and C. F. Lee: U.S.A., Taiwan, and P.R.O.C., patents pending (1997).
34) R. C. Jones: J. Opt. Soc. Am. **31** (1941) 488.
35) R. C. Jones: J. Opt. Soc. Am. **46** (1956) 528.
36) M. Born and E. Wolf: *Principles of Optics* (Pergamon, Oxford, 1980).
37) T. S. Theocaris and E. E. Gdoutos: *Matrix Theory of Photoelasticity* (Springer-Verlag, New York, 1979).
38) T. D. Perng, W. J. Wu, S. J. Chiang, C. K. Lee and C. W. Huang: Proc. of the 4th Natl. Conf. Sci. and Tech. of Natl. Def. Ta-Hsi, Tao-Yuan, Taiwan, November 4, 1995, p. 12.
39) Giin-Yuan Wu and C. K. Lee: Proc. Asia-Pacific Data Storage Conf., Ta-Shee Resort, 1997.

40) Optical Research Associates, 3280 East Foothill Blvd., Pasadena, CA 91107.
41) R. J. Wallace: Bell System Techn. J. (1951) 1145.
42) A. Van Herk: Ph.D. Dissertation, Delft Univ. of Tech., The Netherlands, 1980.
43) R. E. Eaton, K. B. Klaassen and J. C. L. van Peppen: IBM Tech. Discl. Bull. **34** (1991) 430.
44) K. A. Flechsig, C. K. Lee, S. L. Lee, M. L. McGhee, U. V. Nayak, T. C. O'Sullivan and J. Walian: U. S. Patent No. 5,423,207 (1995).
45) K. A. Flechsig, C. K. Lee, S. L. Lee, U. V. Nayak and T. C. O'Sullivan: U. S. Patent No. 5,450,747 (1995).
46) K. A. Flechsig, C. K. Lee, S. L. Lee, U. V. Nayak, and T. C. O'Sullivan: U. S. Patent No. 5,581,021 (1996).
47) T. T. Wu: Inst. Appl. Mech., Non-Destructive Testing Lab., National Taiwan University, Taipei, Taiwan, R.O.C., private communications (1998).
48) T. T. Wu and Y. H. Liu: to be published in Ultrasonics (1998).